

Hierarchical Characteristics of Hydrogen-Assisted Crack Growth and Microstructural Strain Evolution in Tempered Martensitic Steels: Case of Quasi-cleavage Fracture



TINGSHU CHEN, TAKAHIRO CHIBA, MOTOMICHI KOYAMA,
AKINOBU SHIBATA, EIJI AKIYAMA, and KENICHI TAKAI

The local plastic strain evolution associated with crack growth in hydrogen-assisted quasi-cleavage fracture was investigated using tempered lath martensitic steels. The quasi-cleavage crack grew *via* the following process. After crack initiation, the crack grew sharply to a certain length by repeated episodes of nano-void nucleation and coalescence. When the sharp crack tip intersected microstructural boundaries such as a lath or block, crack deflection/branching occurred. This was followed by crack tip blunting, which temporarily stopped crack growth. Further crack growth was possible *via* one of the following two routes: (1) sharp crack initiation/growth from the blunt crack tip, and (2) new crack initiation near the blunt crack tip. The newly formed cracks subsequently coalesced. Repetition of this multi-scale crack growth mechanism finally caused a quasi-cleavage fracture. Correspondingly, hierarchical crack morphologies were observed, which coincided with the lath martensitic microstructures and fractographic features. Furthermore, specific correlations were found between hydrogen-assisted cracking behavior and local plastic strain evolution at different spatial scales. Specifically, the largest plastic strain evolution occurred in the region where crack coalescence was observed. The second largest plastic strain evolution occurred when crack tip blunting occurred. Nanoscale local plasticity evolution around a sharp crack was also observed as an appearance of intense slip bands, indicating that the local plasticity played a key role in the hydrogen-related sharp crack growth.

<https://doi.org/10.1007/s11661-021-06423-1>

© The Minerals, Metals & Materials Society and ASM International 2021

I. INTRODUCTION

MARTENSITIC steel is the most common high-strength low-alloy steel, in part because it exhibits a strength of over 1 GPa and its ductility can satisfy the basic needs for manufacturing. The excellent mechanical properties of martensitic steel are the reason that it is widely used as an industrial material for applications such as automobile components. The crystallography of martensite consists of either a body-centered cubic (BCC) or body-centered tetragonal (BCT) structure, referred to as α' -martensite. Specifically, the major morphology of martensite is lath.^[1] Lath martensite consists of a hierarchical microstructure.^[1–5] The unit of the microstructure is lath with the width of 0.2 to 0.5 μm . A lath tends to align parallel to other laths in a large region of the prior austenite grain. A group of laths with the same orientation is called a block, and a group of several blocks with the same habit plane is called a packet. Both block and packet boundaries are effective martensite structures that act as barriers to dislocation

TINGSHU CHEN is with the Institute for Materials Research, Tohoku University, 2-1-1 Katahira, Aoba-ku, Sendai 980-8577, Japan and also with the Graduate School of Engineering, Tohoku University, 6-6 Aramaki Aza Aoba, Aoba-ku, Sendai, Miyagi, 980-8579, Japan. TAKAHIRO CHIBA is with the Graduate School of Science and Technology, Sophia University Tokyo 102-8554, Japan and is presently with Nippon Steel Co., Amagasaki, Hyogo, Japan. MOTOMICHI KOYAMA is with the Institute for Materials Research, Tohoku University and also with the Elements Strategy Initiative for Structural Materials (ESISM), Kyoto University, Yoshida-honmachi, Sakyo-ku, Kyoto 606-8501, Japan. Contact e-mail: koyama@imr.tohoku.ac.jp AKINOBU SHIBATA is with the Elements Strategy Initiative for Structural Materials (ESISM), Kyoto University and also with the Research Center for Structural Materials, National Institute for Materials Science, 1-2-1 Sengen, Tsukuba 305-0047, Japan. EIJI AKIYAMA is with the Institute for Materials Research, Tohoku University. KENICHI TAKAI is with the Department of Engineering and Applied Sciences, Sophia University, Tokyo 102-8554, Japan.

Manuscript submitted February 24, 2021; accepted August 1, 2021.

Article published online August 17, 2021

motion, which provides the strength and toughness of martensitic steels.^[2,3]

The importance of lath martensite has been increasing because of the recent demand for high-strength steels. However, the introduction of hydrogen into steels is inevitable either in the fabrication process or in service environments; on the other hand, it is well known that the susceptibility to hydrogen embrittlement increases with an increase in the strength of materials. Thus, hydrogen embrittlement as a latent problem for structural materials is particularly serious for high-strength martensitic steels.^[6,7] To prevent hydrogen-induced failure, many attempts have been made to clarify the hydrogen embrittlement micro-mechanisms associated with two prevailing fracture modes: intergranular fracture and quasi-cleavage fracture. The appearance of the fracture modes is dependent on hydrogen charging and deformation conditions, and both fracture modes have been investigated to optimize the design of hydrogen-robust martensitic steels. Among the various micro-mechanisms, hydrogen-enhanced decohesion (HEDE),^[8–13] hydrogen-enhanced localized plasticity (HELP),^[11–15] and hydrogen-enhanced strain-induced vacancy (HESIV)^[13,16–19] have gained the most attention so far. Hydrogen in the HEDE mechanism decreases the cohesive strength at specific microstructures, such as at grain boundaries.^[20] The presence of hydrogen can also reduce the energy required for activating the dislocations, which induces local plasticity that triggers cracking (*i.e.*, the HELP mechanism).^[21] In the case of quasi-cleavage fracture of martensitic steel, both the HEDE and HELP mechanisms have been reported to act as primary mechanisms triggering hydrogen embrittlement.^[22,23] Therefore, in terms of HELP, plasticity evolution and its role in cracking are key to understanding the hydrogen embrittlement micro-mechanism. More specifically, the plasticity mechanism in the hierarchical characteristics of lath martensite is complex even without hydrogen, and the presence of cracks further complicates the evolution behavior of plasticity. Accordingly, the microstructure surrounding cracks in martensitic steels has not yet been fully understood. Therefore, we investigated the behavior of crack-related plasticity mechanisms in lath martensitic steel in the presence of hydrogen to understand the nature of quasi-cleavage fracture.

As for quasi-cleavage fracture in a low-carbon martensitic steel, Nagao *et al.* reported that quasi-cleavage fracture surfaces were caused by failure along lath boundaries.^[23,24] Shibata *et al.* focused on the microstructural and crystallographic features of quasi-cleavage fractures and proposed that the hydrogen-related quasi-cleavage fracture propagated along {011} planes with the lath.^[25–28] These attempts revealed the lath-related cracking path of quasi-cleavage fractures in lath martensite. However, to the best of our knowledge, the specific roles of microstructure and plasticity in the respective multi-scale hydrogen-related crack growth stages (*e.g.*, sharp crack propagation, crack blunting, crack branching/deflection, subcrack initiation, and crack coalescence) are not yet

understood. Therefore, microstructural investigations of the specific quasi-cleavage cracks and related plastic strain evolution are necessary to understand the role of hierarchical characteristics in hydrogen-assisted quasi-cleavage fracture in lath martensite.

Based on the above-mentioned motivation, we selected tempered martensitic steel for the present study. The microstructures and local plasticity around the specific quasi-cleavage cracks were analyzed in bulk specimens using scanning electron microscopy-based techniques, including electron channeling contrast imaging (ECCI) and electron backscatter diffraction (EBSD) analysis. The correlation among the hierarchical martensite structure, crack morphology, local plasticity, and fractographic features were discussed to understand the hydrogen-assisted quasi-cleavage fracture mechanisms.

II. EXPERIMENTAL PROCEDURE

A. Materials

We received tempered martensitic steel with the chemical composition listed in Table I. Some details, including heat treatment, have been presented elsewhere.^[29] The as-received sample shape was cylindrical, and it was machined using a lathe to make a gauge section of the tensile specimen. Figure 1 shows the microstructure before the tensile tests. The microstructure fully consists of martensite, and fine cementite exists both on the grain boundaries and within the grain interior.^[30] The average transverse size of martensite block was 0.9 μm .

B. Mechanical Tests and Hydrogen Charging

Dog-bone-type tensile specimens with gauge dimensions of 5 mm in diameter and 30 mm in length^[31] were tensile-tested at a cross-head displacement rate of 1 mm/min at ambient temperature. Prior to the tests, the tensile specimens were mechanically polished using emery papers #1000 and #2000. Hydrogen charging was conducted before and during tensile tests in an aqueous solution of NaOH (0.1 N) at a current density of 100 A/m². The hydrogen charging prior to the tensile tests was performed at 30 °C for 96 hours. Under these hydrogen charging and deformation conditions, quasi-cleavage fracture has been reported to occur in the present steel.^[30] Two specimens used for measuring the hydrogen content were mechanically polished, and one of them was electrochemically charged with hydrogen in the same solution at the same current density for the tensile test, and the other was used as blank. The hydrogen content was measured by thermal desorption analysis (TDA) using a gas chromatograph with a semiconductor gas sensor as the detector at a heating rate of 100 °C/h. The diffusible hydrogen content, which plays a primary role in hydrogen embrittlement, was defined as the cumulative hydrogen desorbed from ambient temperature to 300 °C.

Table I. Chemical Composition of the Steel Used (Wt Pct)

C	Si	Mn	P	S	Cu	Ti	B	Fe
0.35	1.88	0.73	0.015	0.008	0.02	0.03	0.0024	bal.

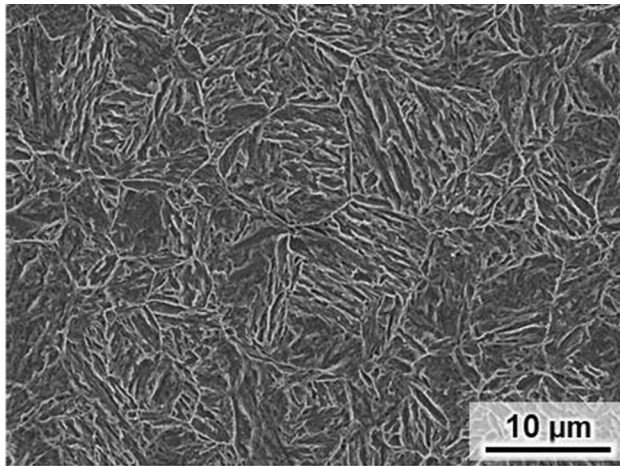


Fig. 1—Microstructure before tensile tests. This image was obtained after chemical etching with 5 pct Nital.

C. Microstructural Characterization

The fracture surface obtained by tensile testing was observed using secondary electron imaging (SEI) at an accelerating voltage of 15 kV. Furthermore, a specimen was prepared by tensile testing, which was interrupted immediately after the ultimate tensile strength (UTS), to characterize the microstructures surrounding the cracks. The microstructures were observed by SEI, ECCI, and EBSD measurements. The specimen for the damage-related microstructural observations was first mechanically ground to obtain a rectangular specimen shape, because ECCI and EBSD require a flat specimen surface. Then, it was mechanically polished to a mirror finish using colloidal silica with a particle size of 60 nm. The ECCI was operated at 30 kV, and EBSD measurements were conducted at 20 kV with a beam step size of 50 nm.

III. RESULTS

A. Mechanical Tests and Fractographic Feature

Figure 2 shows the TDA profiles of the specimens with and without hydrogen-charging. No significant peak was observed in the uncharged specimen, and only a single peak was observed in the hydrogen-charged specimen. The diffusible hydrogen contents of the specimens with and without hydrogen-charging were 0 and 2.9 mass ppm, respectively.

Figure 3 shows engineering stress–strain curves with and without hydrogen charging. Hydrogen charging significantly deteriorated the elongation, but the fracture

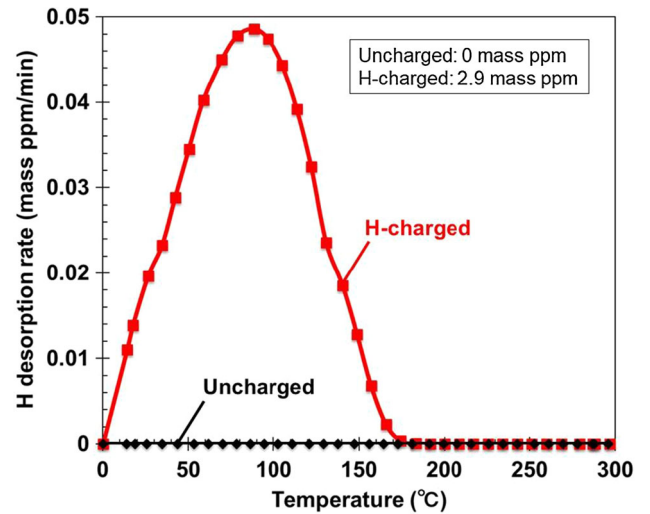


Fig. 2—Hydrogen desorption rate vs. temperature curves.

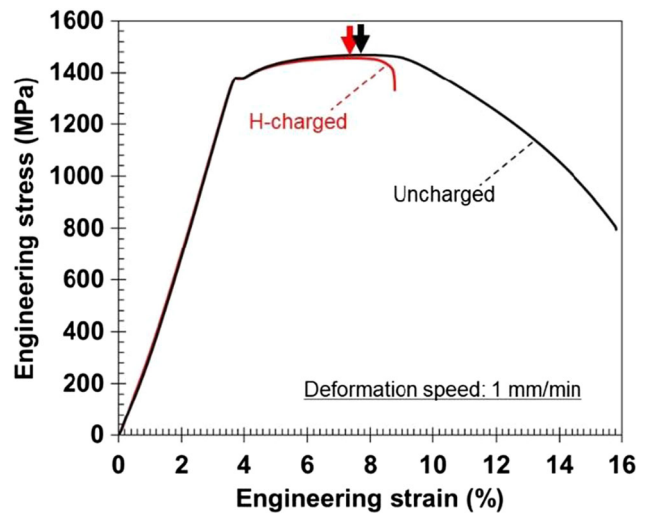


Fig. 3—Engineering stress–strain curves. The black and red arrows indicate UTSs of the specimens without and with hydrogen charging, respectively (Color figure online).

of the hydrogen-charged specimen occurred after significant plastic deformation.

Figure 4 shows the fracture surface of the hydrogen-uncharged specimen. The fracture surface was covered with dimples, which indicates that the failure of the hydrogen-uncharged specimen was caused by typical ductile fracture *via* micro-void coalescence. There were two types of micro-voids in Figure 4(a). The first type whose size was larger than 10 μm , included an inclusion, which is called fish-eye, as shown in Figure 4(b). This indicates that the first type of dimple was formed *via* cracking at the matrix/inclusion interfaces. The other type was smaller than the first type (less than 5 μm) and did not contain fish-eye. This type of dimple can be formed by lattice defect accumulation at microstructure boundaries such as grain boundary.

The hydrogen-charged specimen exhibited a quasi-cleavage fracture, as shown in Figure 5. A quasi-cleavage fracture was initiated from the inclusion

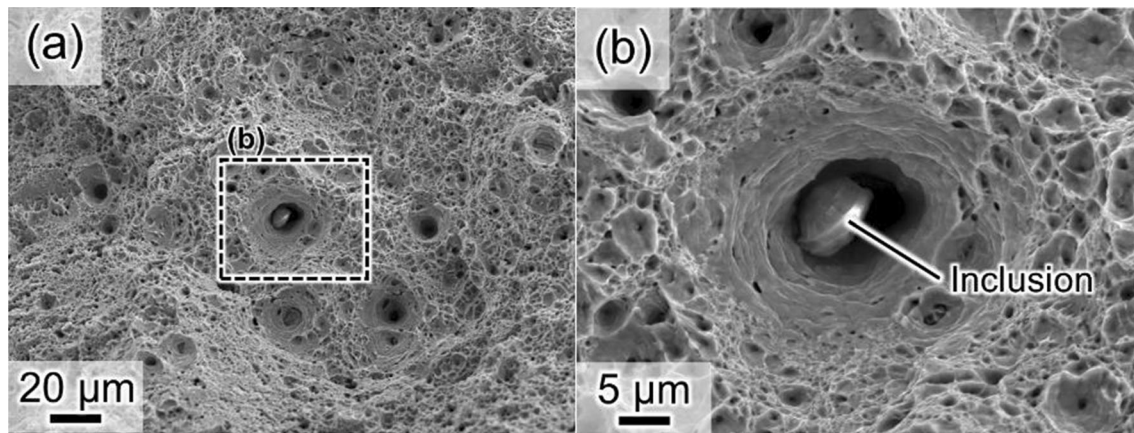


Fig. 4—(a) Micro-void coalescence phenomenon obtained by tensile testing without hydrogen charging, and (b) the same sample at higher magnification.

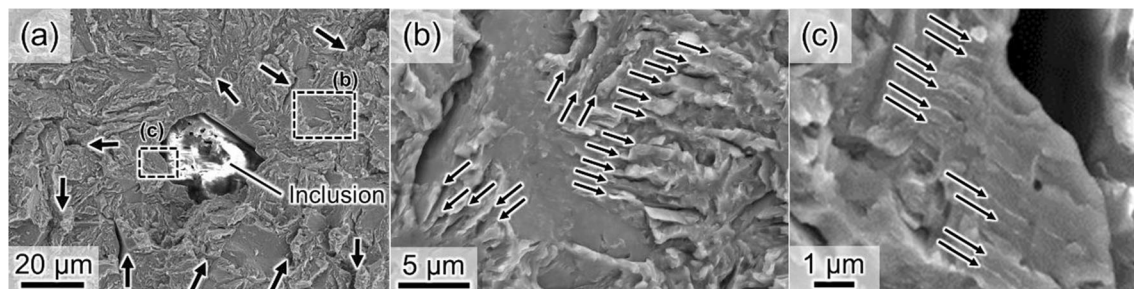


Fig. 5—(a) Quasi-cleavage fracture surface obtained by tensile testing, (b) and (c) the same sample at higher magnification. The arrows indicate cliffs, river-like patterns, and shallow striations in (a through c), respectively.

[e.g., $\text{Al}_2\text{O}_3\text{-(CaO)}_x$ type]. Furthermore, there were three types of features with different spacing scales on the fracture surface. In the low-magnification image (Figure 5(a)), deep cracks or cliff-like steps were observed, as indicated by arrows, which are hereafter referred to as a cliff. The spacing of the cliffs was approximately a few dozen micrometers, which was similar to the prior austenite grain size. River-like patterns were also observed on the facets of quasi-cleavage fracture in Figure 5(b), and the average spacing of the pattern was $1.0\ \mu\text{m}$, which was close to the transverse size of the block. When the quasi-cleavage facet near the inclusion was magnified (Figure 5(c)), dense shallow striations with a spacing on a sub-micrometer scale were observed, which were regularly ordered on the fracture facet.

B. Crack Morphology and Local Strain Evolution

To understand the relationship between the hierarchical fractographic characteristics, another tensile test for the hydrogen-charged specimen was interrupted immediately after reaching the UTS. Next, internal quasi-cleavage cracks and their surrounding microstructures were observed. Figures 6(a) and 6(b) show the specimen configuration after mechanical polishing and a low-magnification image of the cracks, respectively. The black dots in Figure 6(b) indicate the presence of

numerous voids associated with the inclusions and pitting corrosion. The primary crack initiation site was an inclusion or its associated void. The non-inclusion area also showed cracks as minor crack initiation sites.

Figure 7(a) shows another example of a low-magnification image, indicating relatively larger cracks than those in Figure 6(b). Obvious crack tip blunting was observed, which involved plastic strain evolution, as evident in the kernel average misorientation (KAM) map (Figure 8(a)) that corresponds to the geometrically necessary dislocation density and related plastic strain.^[32,33] Crack tip blunting stopped crack growth. Note that micro-scale cracks formed near the blunt crack tip. The size of the newly formed crack was on the order of a few dozen micrometers. As evident in Figure 7(b), the largest and second-largest cracks in the image coalesced with each other. The region where crack coalescence was observed is magnified, as shown in Figure 7(c). Because the crack coalescence region was barely open and its crack surface was nearly parallel to the loading direction, crack coalescence occurred *via* plastic shear deformation in the ligament of the two adjacent blunt crack tips. Correspondingly, the evolution of the largest local strain was observed in the crack coalescence region, as shown in the KAM map (Figure 8(a)). It is also worth noting in Figure 7(c) that micron-scale crack branching and deflection occurred. The branches of the crack were parallel to the lath/block

alignment (Figure 8(b)), and their spacing was similar to the spacing of the river-like patterns on the fracture surface in Figure 5(b). According to the crystallographic analysis of martensite variant (Figure 8(c)), the crack blunting occurred when its tip reached the prior austenite grain boundary.

Sharp crack growth also occurred, which was observed ahead of the blunt small crack tip, as highlighted by the black-dashed square in Figure 7(b). Local

strain evolution involved in the sharp crack growth was also exhibited in the KAM map (Figure 8(a)). Note that the KAM values surrounding the sharp crack were lower than those associated with the crack tip blunting and crack coalescence. The low KAM values indicate the degree of plastic strain evolution during the sharp crack growth was small or the size of the localized plasticity was smaller than the spatial resolution of the EBSD measurement. To clarify the details of the local plasticity, the highlighted region in Figure 7(b) was observed using ECCI in high magnification, as shown in Figure 9. The crack grew transgranularly from the blunt crack tip without distinct blunting, branching, and deflection. Slip bands were observed around the sharp crack, as indicated by the black arrows in Figure 9(b), and the size of the thin deformation band spacing was on a sub-micron scale.

C. Microstructure and Nano-voids Near a Crack Tip

There were two types of quasi-cleavage crack growth. Figure 10 shows an ECC image that depicts the sharp crack growth along the lath/block alignment. More specifically, an obvious crack deflection occurred when the lath/block alignment direction changed (marked by a black-dashed rectangle) and then the crack started to grow along the lath/block alignment. According to the RD-IPF map (inset of Figure 10), the crystallographic orientation features of the blocks around the crack path were exhibited clearly, suggesting the quasi-cleavage crack grew on or near the block boundary.

The other type was crack growth across the lath/block, as shown in Figure 11(a). A magnification of the crack tip (Figure 11(b)) showed that there was a micron-scale subcrack, and tiny voids existed in the ligament of the two cracks. The ligament region is further magnified in Figure 11(c). The crack growth was impeded by the lath/block boundary, which is marked by the black-dashed lines in the figure. The crack tips, which were blocked at the lath/block boundaries, showed nano-scale crack tip blunting. Furthermore, some black dots were observed in the ECC image. Since the black dots were observed also in the SE image in Figure 11(d), they were nano-voids that formed inside the lath/block.

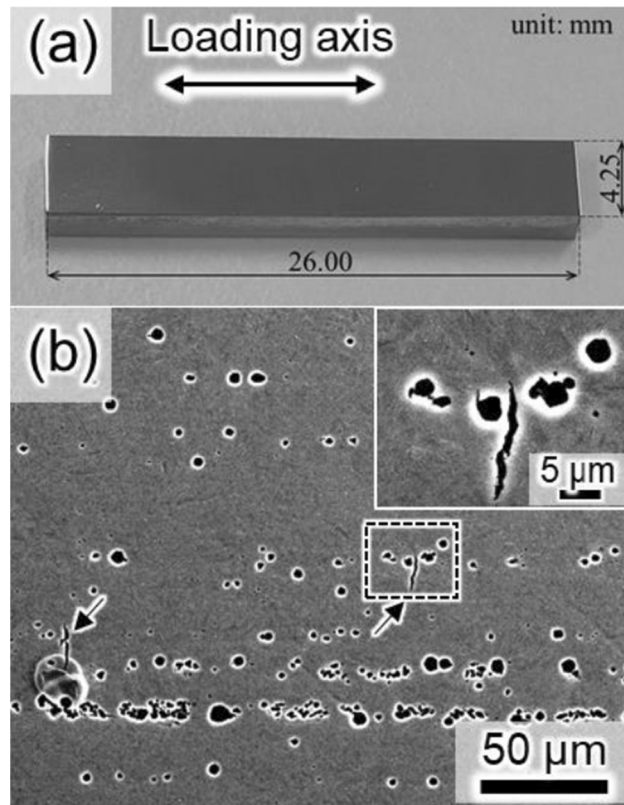


Fig. 6—(a) Overview of the mechanically polished hydrogen-charged tensile test specimen. (b) A low-magnification image of the same polished specimen surface (SE image). The arrows indicate some cracks. The inset indicates a magnification that shows cracks initiated from inclusions and the non-inclusion area.

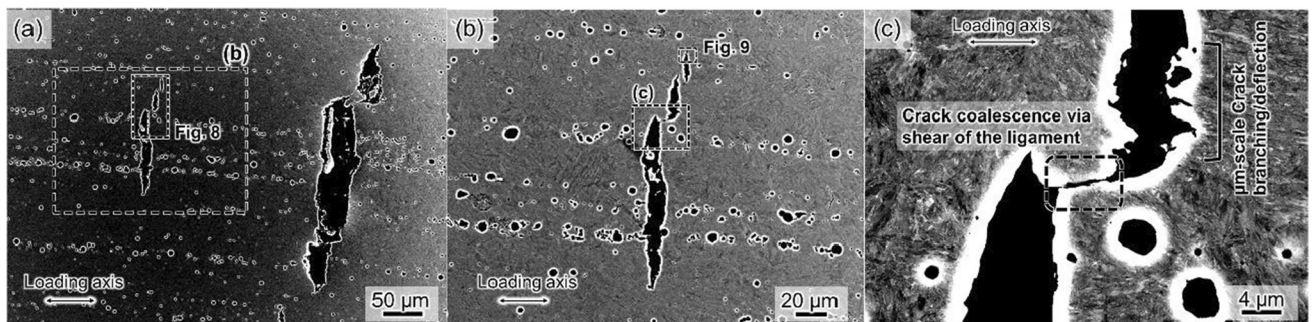


Fig. 7—(a) ECC image showing small cracks near the relatively large cracks. (b) Magnification of the highlighted region in (a). (c) Magnified ECC image of the highlighted region in Fig. (b), showing micron-scale crack branching/deflection and shear-induced crack coalescence.

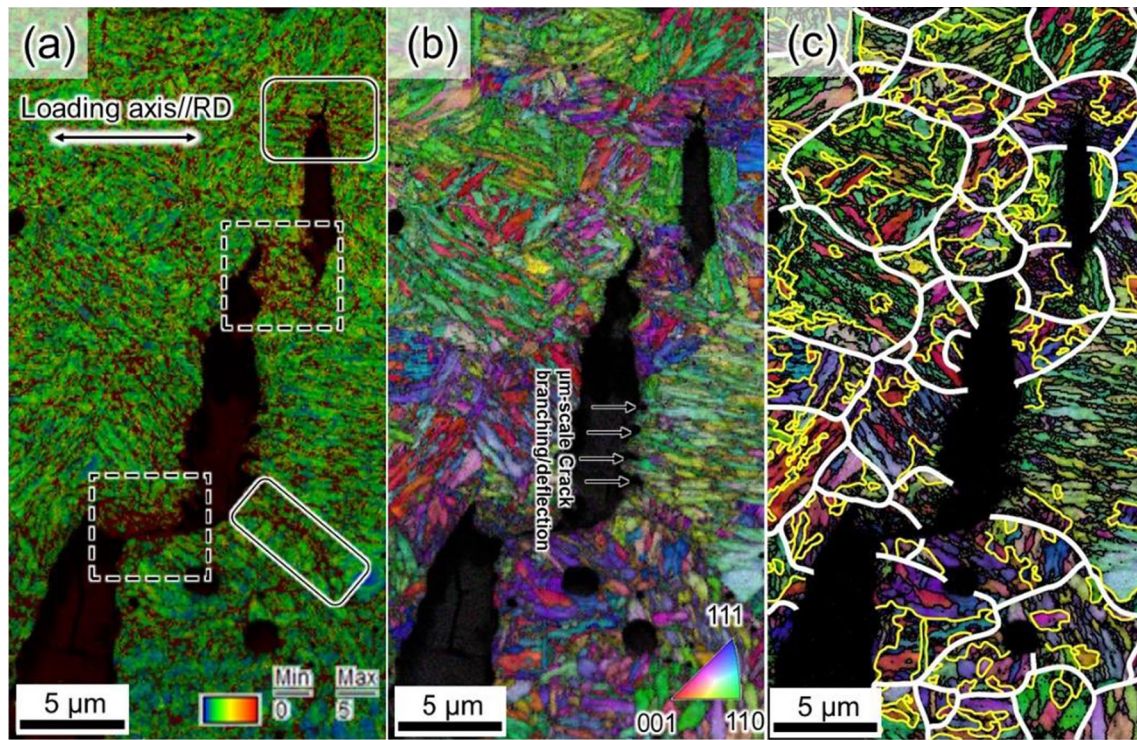


Fig. 8—(a) KAM and (b) RD-IPF maps of the region corresponding to Fig. 7(b). (c) Identification of martensite boundary. The confidence indexes of the data shown here are higher than 0.1. The yellow and white lines indicate packet and prior austenite grain boundaries, respectively. The boundaries having misorientations of > 5 deg are indicated by the black lines in (c) (Color figure online).

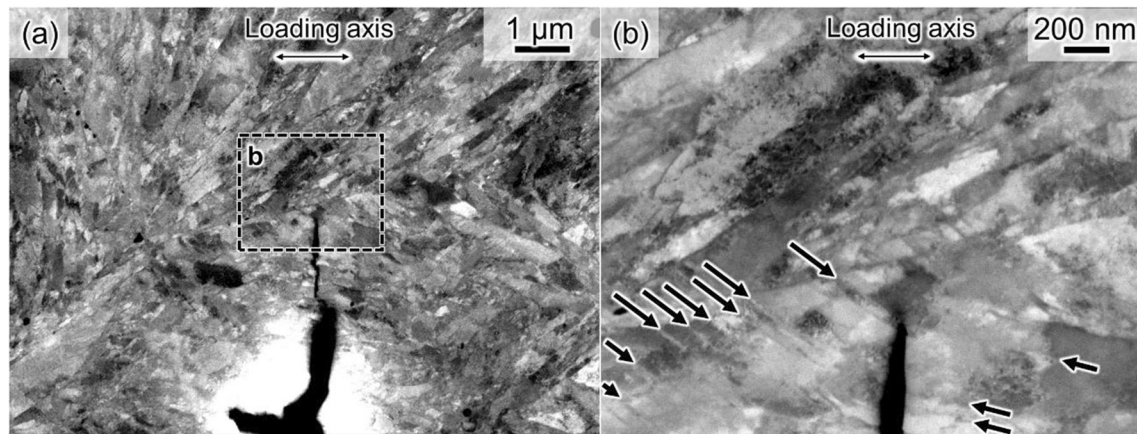


Fig. 9—(a) Another magnified ECC image of Fig. 7(b), showing formation of a sharp crack at the tip of blunted crack. (b) Highly magnified ECC image of the highlighted region in (a). The arrows indicate the presence of deformation bands.

IV. DISCUSSION

A. Hierarchical Characteristics of the Fracture Surface and Crack Morphology

According to the fractography analysis in Figures 4 and 5, the damage was preferentially formed around the inclusion in both hydrogen-charged and non-charged specimens, and for the hydrogen-related crack, it subsequently propagated in a quasi-cleavage fracture mode. Three types of morphological features: cliffs, river-like patterns, and shallow striations, each with different

spacing scales existed on the fracture surface. A similar faceted fracture surface was also observed in a previous study.^[27] These features are highly relevant to the hierarchical features of the microstructure and crack morphology. Specifically, the spacing between these cliffs was a few dozen microns (*e.g.*, the average size of the cliff spacings in Figure 5(a) was $30 \mu\text{m}$), which was similar to the size of the cracks that formed near the blunt crack tips (about $30 \mu\text{m}$ measured in Figure 7(b)). In other words, we attributed the formation of cliffs to crack coalescence, as schematically shown in Figure 12(a).

The river-like pattern spacing was approximately $1.0\ \mu\text{m}$ (Figure 5(b)), which was close to the transverse size of the block. The occurrence of the river-like pattern, a typical feature of quasi-cleavage fracture,^[6] was related to the crack branching/deflection at martensite

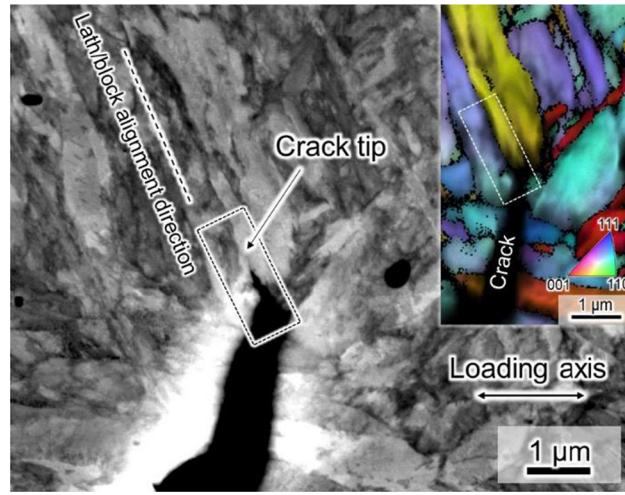


Fig. 10—ECC image showing crack growth along the lath/block alignment direction. The inset indicates the RD-IPF map of the highlighted region in the ECC image.

boundaries, such as lath/block boundaries and prior austenite grain boundaries, instead of originating from fine tear ridges caused by failure along the intense slip bands.^[22,34] When the crack grew within a prior austenite grain under tensile stress, the block and lath boundaries prevented its extension (Figure 8). Once the crack growth was blocked by block/lath boundaries, crack branching or deflection occurred along the lath/block alignment. Therefore, the river-like pattern formation as a result of crack branching/deflection occurred with a relatively constant spacing that corresponded to the transverse size of the block (Figure 12(b)). The link between the crack quasi-cleavage facets and the martensite lath structure has been reported in another martensitic steel.^[35]

The shallow striations were regularly ordered on the quasi-cleavage fracture facet and the spacing between them was sub-micron in scale, similar to the transverse size of the lath (Figure 5(c)). Therefore, the distribution of the shallow striations is attributed to the arrangement of the lath. Specifically, the location of the shallow striations was rather near to the inclusion. Since the crack initiated around the inclusion, the region covered with shallow striations corresponds to the initial stage of the quasi-cleavage crack growth. The initial crack growth behavior was also exhibited in Figure 9. A newly sharp crack was formed from the blunt crack tip, and fine slip bands were observed around the sharp

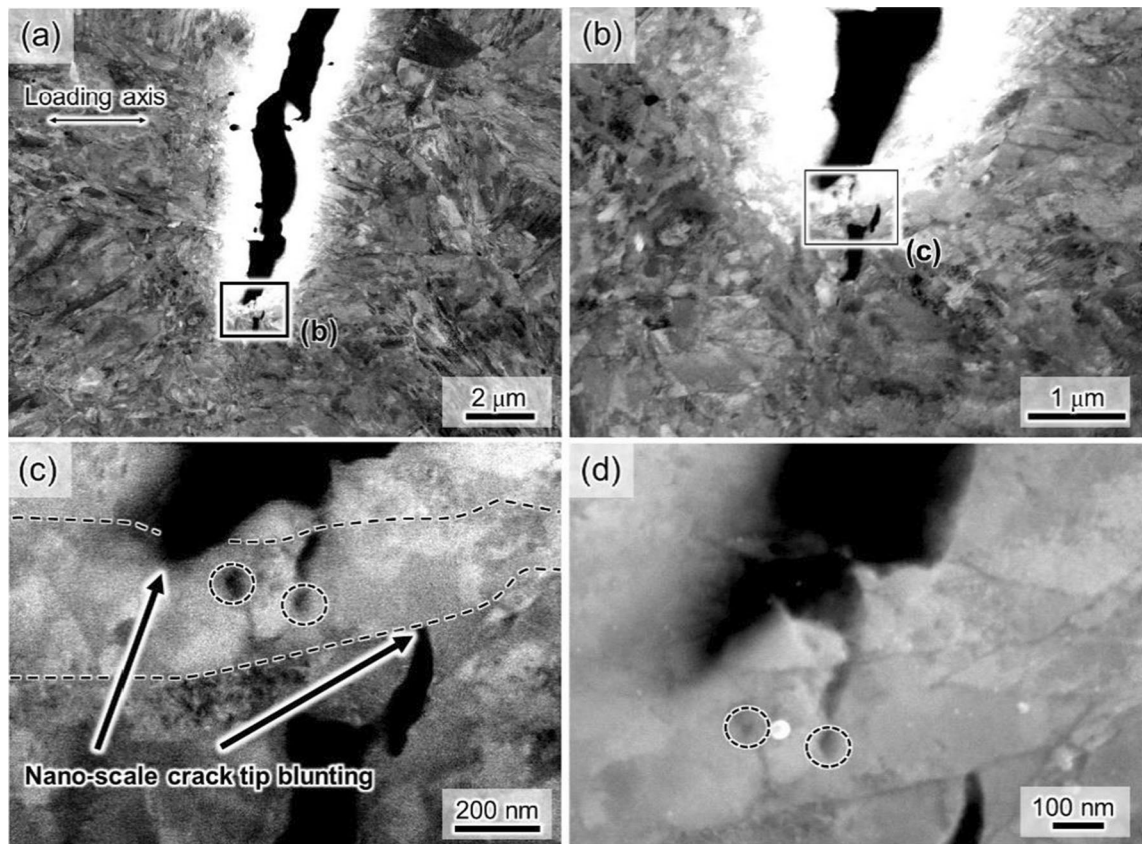


Fig. 11—ECC images showing (a) an overview of a crack, and (b, c) magnifications of the crack tip. (d) SE image of the crack tip and nano-void. The circles in (c, d) indicate nano-voids, and the dashed lines in (c) indicate the lath/block boundary.

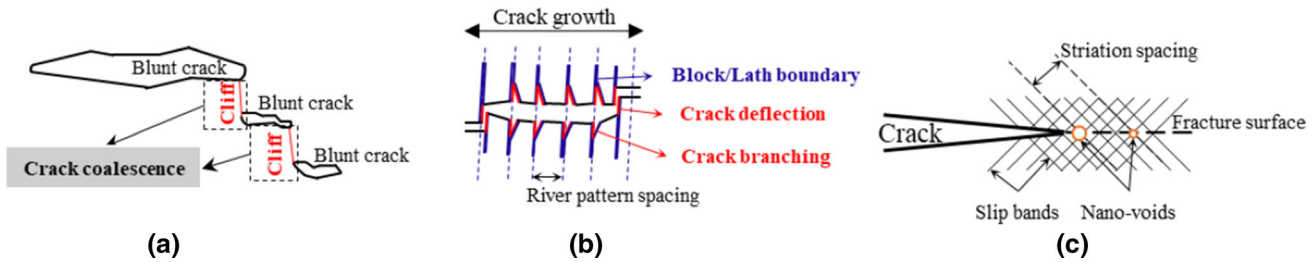


Fig. 12—Schematic representations of the relationships between different crack morphologies and three typical features on the fracture surface: (a) cliffs, (b) river-like patterns, and (c) shallow striations.

crack path. It has been reported that localized slip near a crack tip induces nano-void nucleation.^[36–38] When this nano-void grew to a threshold size, it coalesced with the crack. Repetition of this process enabled crack growth without a large crack opening, which resulted in shallow striations on the fracture facet. However, it is worth noting that, although the stress concentration occurred at the intersection of localized slips, all the slip band intersections would not always fulfil the criteria of nano-void nucleation due to the probabilistic phenomena such as local hydrogen trap/accumulation, and interactions with pre-existing defects. For instance, in Figure 11, although the transverse size of the lath/block was much larger than the slip band spacing, only two nano-voids/cracks appeared within the lath/block. Since the lath is the unit microstructure of lath martensite, the growth of the quasi-cleavage crack would be mainly obstructed by the lath in the initial stage.^[39,40] Concerning that a limited number of localized slip intersections could nucleate nano-voids within a lath, the spacing of shallow striations exhibited the similarity to the transverse size of the lath. Cho *et al.* also attributed the fine features (*i.e.*, the shallow striations in this study) to the arrangement of the lath in their recent research.^[35] Consequently, in the present study, the repetition process of nano-void nucleation and coalescence induced the shallow striations with a spacing similar to the transverse size of the lath, as schematically shown in Figure 12(c).

Based on the present interpretations, the hydrogen-assisted crack growth process can be described as follows. First, a crack is initiated from inclusions, and then sharply grows to a certain length *via* the repetition of nano-void nucleation and coalescence. When the sharp crack growth mechanism cannot continuously function at microstructural boundaries such as the block, crack tip deflection or branching occurs. When the crack cannot grow even after crack deflection/branching, crack tip blunting occurs mainly near prior austenite grain boundaries, which temporarily stops the crack growth. Then, the blunt crack re-grows *via* one of two routes. The first route is the restart of the sharp crack growth from the blunt crack tip. The second route is new crack initiation around the blunt crack tip. The newly formed cracks subsequently result in crack coalescence. Repetition of this multiscale crack growth mechanism finally causes a quasi-cleavage fracture. The remaining issues in understanding the quasi-cleavage fracture mechanism are (1) the contribution of plasticity

and (2) the nano-void nucleation mechanism. The former and latter are discussed in Sections IV–B and IV–C, respectively.

B. Plastic Strain Evolution Associated with Three Crack Extension Steps

In terms of plasticity, there are three types of evolution of local plastic strain related to crack extension in hydrogen-charged tempered lath martensitic steels. The largest plasticity evolution was observed in the crack coalescence region (Figure 8(a)). As discussed in Section IV–A, hydrogen-related crack growth requires crack initiation around a large crack tip and subsequent crack coalescence. The large plastic strain indicates that crack coalescence resulted from plastic shear in the ligament between the cracks (Figure 13(a)). Therefore, the well-known hydrogen effect, that is, HELP, promoted crack coalescence.

The second largest plasticity evolution was observed at the tip of the blunt crack, as shown in the KAM map (Figure 8(a)). That is, when crack tip blunting occurred at a martensite boundary such as the prior austenite grain, significant local plasticity evolved, but this plastic strain evolution was not attributed to the hydrogen effect. The evolution of the crack tip strain during crack blunting must appear when hydrogen-related sharp crack growth could not occur (Figure 13(b)).

The third type of local plasticity evolution was observed in the ECCI technique (Figure 9) but was not detected in the KAM map (Figure 8(a)). The contribution of this local plasticity is key to understanding the underlying hydrogen effect on crack growth. The region marked by the black rectangle in Figure 8(a) shows a sharp crack growth from the blunt crack tip. In the corresponding IPF map (Figures 8(b) and (c)), before the sharp crack formation, crack tip blunting occurred near the prior austenite grain boundary, preventing crack growth. Although crack tip blunting temporarily decreased the local stress, work hardening and hydrogen diffusion to the blunt crack tip proceeded with time, which enabled the restarting of sharp crack growth. Once the sharp crack growth restarted, slip band evolution ahead of the sharp crack tip occurred (Figure 13(c)), as observed in the ECC images (Figure 9), which resulted in nano-void nucleation and associated successive sharp crack growth until the crack tip met another martensite boundary. Plasticity-controlled sharp crack growth was observed only in

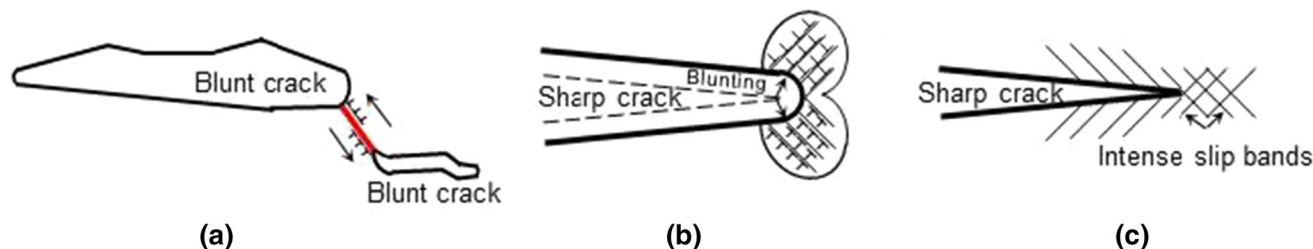


Fig. 13—Schematic representations of the relationships between local plastic strain evolution and three different hydrogen-assisted cracking behaviors: (a) crack coalescence, (b) crack tip blunting, and (c) the growth of a sharp crack.

the case of the hydrogen-charged specimen of the tempered martensitic steels. Therefore, the effect of hydrogen on the dislocation behavior at the sharp crack tip was the nature of hydrogen embrittlement. An exception to the case for sharp crack growth occurred when the lath/block alignment was parallel to the crack growth path, as shown in Figure 10. Further details of the nano-void nucleation and associated sharp crack growth are discussed in the next section.

C. Nano-scale Quasi-cleavage Crack Growth

The remaining issue for hydrogen-assisted quasi-cleavage fracture is the sharp crack growth mechanism involving the plasticity effect. Two different crack growth paths for quasi-cleavage fracture were observed in the present study: along the lath/block alignment and in a trans-lath manner. A crack growth path along the lath/block alignment was observed when the lath/block alignment was significantly inclined toward the loading direction. In this case, it has been suggested that the interaction between enhanced slip systems and lath boundaries plays a key role.^[22,24] The slip systems can be activated by macroscopic and crack tip stresses in individual grains with the assistance of hydrogen, in which dislocation motion can be further enhanced by hydrogen (*i.e.*, the HELP mechanism). Furthermore, hydrogen can be transported by dislocations, *i.e.*, hydrogen redistribution in plasticity processes, which results in hydrogen accumulation at or near lath/block boundaries. The locally distributed hydrogen can weaken the cohesive energy or further localize the plasticity along the lath/block boundaries, which causes sharp crack growth. Nagao *et al.* proposed a synergistic mechanism called hydrogen-enhanced plasticity-mediated decohesion to explain hydrogen-induced quasi-cleavage fracture in lath martensite.^[22] Shibata *et al.*^[26,27] proposed that the hydrogen-assisted transgranular crack grew and propagated along typical crystallographic planes (*i.e.*, $\{011\}$ planes) rather than the lath boundaries based on orientation analysis using EBSD. Although the specific cracking paths were different in these studies than in the present study, the hydrogen-enhanced local slips commonly play an instrumental role in the growth of quasi-cleavage cracks along the lath/block alignment direction.

When the crack grows across the lath/block, the lath/block alignment is nearly parallel to the loading direction. Sharp crack growth *via* void nucleation occurs

in this case. As shown in Figures 11(c) and (d), the nucleation of nano-voids occurred within the lath/block, serving as the onset of further transgranular crack growth and propagation. Before discussing the mechanism dominating the nucleation of the nano-voids, it is worth examining the microstructural location of these nano-voids. In terms of hydrogen distribution, the tensile hydrostatic stress gradient can be a reason for nano-void nucleation within a lath/block and at a certain distance from the crack tip.^[41] Once the specimen undergoes tensile loading, the maximum hydrostatic stress at which the hydrogen content reaches its maximum is located at a certain distance from the crack tip,^[41,42] which can be within lath/block. Another factor controlling the void nucleation site is local dislocation motion. As discussed in Section IV-B, the intersection of two slip bands can play a role in transgranular crack/void initiation. The intersections of slip bands provide vacancy,^[16,18,36,43] sessile dislocations^[35,44] and further concentrated hydrogen, which results in an atomistic stress concentration and a reduction in cohesive energy. Because the dislocation microstructure forms within the lath/block and in front of the crack tip, the nano-void nucleates in the lath/block a slight distance from the crack tip. Moreover, the void nucleation site can be the fine inclusions/cementite within the lath, because they can act as significant hydrogen trapping sites and barriers against dislocation motion, which may induce the crack initiation.^[22,35,44] These three competing factors propound an identical result that the nano-voids prefer to nucleate inside the lath/block rather than at the blunt crack tip or on the lath/block boundaries.

Based on the above discussion, the driving mechanism of the nano-void nucleation and associated sharp crack growth is schematically shown in Figure 14. A high hydrogen concentration appeared inside the lath/block at some distance from the crack tip during nano-scale crack tip blunting (observed in Figure 11(c)) and subsequent tentative non-propagation period (Figure 14(a)). The presence of hydrogen promoted the interaction of the slip bands. Although the present analysis could not determine the active slip system at the crack tip, a previous study reported that slip on two different $\{112\}$ planes would be key to inducing crack/void nucleation.^[35] The intersections of these slip bands are favorable sites for nano-void nucleation due to locally high concentrations of hydrogen, stress, and vacancies. Once the local stress state elevated to the threshold value with the assistance of hydrogen,

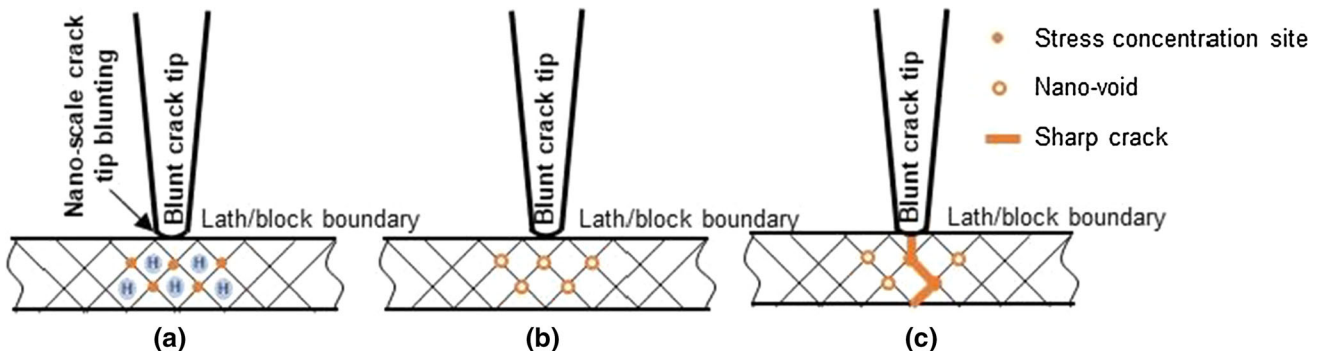


Fig. 14—Schematic illustrations of the mechanism of quasi-cleavage fracture growth in a trans-lath mode: (a) hydrogen accumulation inside the lath/block during nano-scale crack tip blunting, (b) nano-void nucleation, and (c) the coalescence of nano-voids forming sharp cracks within the lath/block.

nano-voids were formed, as shown in Figure 14(b). These nano-voids increased in size until coalescence occurred with the adjacent voids. Crack/void coalescence then caused sharp crack growth inside the lath/block (Figure 14(c)). Considering the present results with those of previous studies, two types of sharp crack growth along the lath/block and across the lath/block can occur on $\{110\}$ (along the lath/block alignment)^[27] and $\{001\}$ (the intersecting plane of two different $\{112\}$ slip bands),^[35] respectively.

V. CONCLUSIONS

In this study, we characterized the hierarchical features of the fracture surface, crack morphology, and strain distribution in hydrogen-charged tempered martensitic steel, based on fractographic analysis and ECCI/EBSD observations of microstructures surrounding internal cracks. First, the correlation between the three typical features on the fracture surface and the specific crack morphologies was clarified. Next, the relationship between the local plastic strain evolution and hydrogen-assisted cracking behavior was investigated. The major conclusions are:

1. Crack growth occurred *via* crack initiation, crack deflection/branching, crack blunting, new crack initiation near the large crack (or sharp crack growth restarts from the blunt crack tip), and crack coalescence. Corresponding to the multi-stage crack growth, there were three typical fractographic features: deep cracks or large steps (referred to as cliffs), river-like patterns, and shallow striations. The cliffs were the result of crack coalescence; the river-like patterns were induced by crack branching/deflection along block/lath boundaries; the shallow striations on fracture facets were related to the nano-void nucleation during sharp crack growth.
2. Crack blunting, branching, and deflection occurred when the crack met the martensite boundaries, such as the lath/block and prior austenite grain

boundaries. The micron-scale crack tip blunting occurred near the prior austenite grain boundaries. The micron-scale crack branching/deflection and nano-scale crack tip blunting occurred at the lath/block boundaries.

3. The largest plastic strain evolution corresponded to crack coalescence, which arose from the plastic shear deformation at the ligament between two blunt crack tips. The second largest plastic strain evolution occurred at the blunt crack tip. Local slip band formation was also observed in ECCI imaging, but it was not detected by the EBSD-KAM analyses. The intense slip bands were the key to the sharp crack growth.
4. Through ECCI observation, two different fracture paths of the hydrogen-assisted quasi-cleavage fracture in the lath martensitic steel were found along the lath/block alignment and the trans-lath direction. The factor controlling the crack path was the lath/block alignment in the loading direction. Specifically, when the lath/block was aligned parallel or nearly parallel to the loading direction, crack growth occurred across the lath/block. When the lath/block was significantly inclined toward the loading direction, the crack path was along the lath/block boundary.
5. Nano-void nucleation within the lath/block was observed at a certain distance from the slightly blunt crack tip. This indicates that the crack growth process of the quasi-cleavage fracture was discontinuous even at the nanoscale level.

ACKNOWLEDGMENTS

This work was supported financially by JSPS KAKENHI (JP20H02457) and a research project entitled “Mechanism from incubation period to fracture in hydrogen embrittlement of high-strength steels” and funded by the Iron and Steel Institute of Japan (ISIJ).

CONFLICT OF INTEREST

On behalf of all authors, the corresponding author states that there is no conflict of interest.

REFERENCES

1. G. Krauss and A.R. Marder: *Metall. Trans.*, 1971, vol. 2, pp. 2343–57.
2. Y. Tomita and K. Okabayashi: *Metall. Trans. A*, 1986, vol. 17, pp. 1203–09.
3. S. Morito, H. Tanaka, R. Konishi, T. Furuhashi, and T. Maki: *Acta Mater.*, 2003, vol. 51, pp. 1789–99.
4. C.A. Apple, R.N. Caron, and G. Krauss: *Metall. Trans.*, 1974, vol. 5, pp. 593–99.
5. S. Morito, X. Huang, T. Furuhashi, T. Maki, and N. Hansen: *Acta Mater.*, 2006, vol. 54, pp. 5323–31.
6. S. Lynch: *Corros. Rev.*, 2012, vol. 30, pp. 105–23.
7. M. Nagumo: *Fundamentals of Hydrogen Embrittlement*, 1st ed., Springer, Tokyo, 2016.
8. Z.D. Harris, S.K. Lawrence, D.L. Medlin, G. Guetard, J.T. Burns, and B.P. Somerday: *Acta Mater.*, 2018, vol. 158, pp. 180–92.
9. J. Li, C. Lu, L. Pei, C. Zhang, R. Wang, and K. Tieu: *Comput. Mater. Sci.*, 2019, vol. 165, pp. 40–50.
10. A. Tehrani, X. Zhou, and W.A. Curtin: *Acta Mater.*, 2020, vol. 185, pp. 98–109.
11. R.A. Oriani and P.H. Josephic: *Acta Metall.*, 1974, vol. 22, pp. 1065–74.
12. I.M. Robertson, P. Sofronis, A. Nagao, M.L. Martin, S. Wang, D.W. Gross, and K.E. Nygren: *Metall. Mater. Trans. B*, 2015, vol. 46B, pp. 1085–1103.
13. O. Barrera, D. Bombac, Y. Chen, T.D. Daff, E. Galindo-Nava, P. Gong, D. Haley, R. Horton, I. Katzarov, J.R. Kermode, C. Liverani, M. Stopher, and F. Sweeney: *J. Mater. Sci.*, 2018, vol. 53, pp. 6251–90.
14. H.K. Birnbaum and P. Sofronis: *Mater. Sci. Eng. A*, 1994, vol. 176, pp. 191–202.
15. T. Matsumoto, J. Easman, and H.K. Birnbaum: *Scripta Mater.*, 1981, vol. 15, p. 5.
16. Y. Sugiyama and K. Takai: *Acta Mater.*, 2021, vol. 208, p. 116663.
17. M. Nagumo: *Mater. Sci. Technol.*, 2004, vol. 20, pp. 940–50.
18. K. Takai, H. Shoda, H. Suzuki, and M. Nagumo: *Acta Mater.*, 2008, vol. 56, pp. 5158–67.
19. M. Nagumo and K. Takai: *Acta Mater.*, 2019, vol. 165, pp. 722–33.
20. A. Tehrani and W.A. Curtin: *ICF 2017 14th Int. Conf. Fract.*, 2017, vol. 1, pp. 644–45.
21. Z. Tarzimaghadam, D. Ponge, J. Klöwer, and D. Raabe: *Acta Mater.*, 2017, vol. 128, pp. 365–74.
22. A. Nagao, M. Dadfarnia, B.P. Somerday, P. Sofronis, and R.O. Ritchie: *J. Mech. Phys. Solids*, 2018, vol. 112, pp. 403–30.
23. A. Nagao, C.D. Smith, M. Dadfarnia, P. Sofronis, and I.M. Robertson: *Acta Mater.*, 2012, vol. 60, pp. 5182–89.
24. A. Nagao, C.D. Smith, M. Dadfarnia, P. Sofronis, and I.M. Robertson: *Procedia Mater. Sci.*, 2014, vol. 3, pp. 1700–05.
25. A. Shibata, H. Takahashi, and N. Tsuji: *ISIJ Int.*, 2012, vol. 52, pp. 208–12.
26. A. Shibata, T. Matsuoka, A. Ueno, and N. Tsuji: *Int. J. Fract.*, 2017, vol. 205, pp. 73–82.
27. A. Shibata, T. Murata, H. Takahashi, T. Matsuoka, and N. Tsuji: *Metall. Mater. Trans. A*, 2015, vol. 46A, pp. 5685–96.
28. A. Shibata, Y. Momotani, T. Murata, T. Matsuoka, M. Tsuboi, and N. Tsuji: *Mater. Sci. Technol. (UK)*, 2017, vol. 33, pp. 1524–32.
29. M. Yu and T.E. Power: *ISIJ Int.*, 2013, vol. 13086, pp. 1–4.
30. K. Ogawa, Y. Matsumoto, H. Suzuki, and K. Takai: *ISIJ Int.*, 2019, vol. 59, pp. 1705–14.
31. M. Ohori, T. Chiba, Y. Matsumoto, H. Suzuki, and K. Takai: *IOP Conf. Ser. Mater. Sci. Eng.*, 2018, vol. 461, p. 012062.
32. M. Calcagnotto, D. Ponge, E. Demir, and D. Raabe: *Mater. Sci. Eng. A*, 2010, vol. 527, pp. 2738–46.
33. S. Dejan: *Process. Appl. Ceram.*, 2012, vol. 6, pp. 1–13.
34. M.L. Martin, J.A. Fenske, G.S. Liu, P. Sofronis, and I.M. Robertson: *Acta Mater.*, 2011, vol. 59, pp. 1601–06.
35. L. Cho, P.E. Bradley, D.S. Lauria, M.L. Martin, M.J. Connolly, J.T. Benzinger, E.J. Seo, K.O. Findley, J.G. Speer, and A.J. Slifka: *Acta Mater.*, 2021, vol. 206, p. 116635.
36. T. Neeraj, R. Srinivasan, and J. Li: *Acta Mater.*, 2012, vol. 60, pp. 5160–71.
37. T.T. Huynh, M. Koyama, Y. Takahashi, S. Hamada, K. Tsuzaki, and H. Noguchi: *Scripta Mater.*, 2020, vol. 178, pp. 99–103.
38. D. Asari, S. Mizokami, M. Fukahori, and K. Takai: *Mater. Sci. Eng. A*, 2020, vol. 780, p. 139209.
39. T. Ohmura, A.M. Minor, E.A. Stach, and J.W. Morris: *J. Mater. Res.*, 2004, vol. 19, pp. 3626–32.
40. L. Morsdorf, O. Jeannin, D. Barbier, M. Mitsuhara, D. Raabe, and C.C. Tasan: *Acta Mater.*, 2016, vol. 121, pp. 202–14.
41. A. Laureys, T. Depover, R. Petrov, and K. Verbeken: *Mater. Sci. Eng. A*, 2017, vol. 690, pp. 88–95.
42. P. Doig: *Mater. Sci. Eng.*, 1981, vol. 48, pp. 181–88.
43. K. Saito, T. Hirade, and K. Takai: *Metall. Mater. Trans. A*, 2019, vol. 50A, pp. 5091–5102.
44. D. Guedes, L. Cupertino Malheiros, A. Oudriss, S. Cohendoz, J. Bouhattate, J. Creus, F. Thébault, M. Piette, and X. Feaugas: *Acta Mater.*, 2020, vol. 186, pp. 133–48.

Publisher's Note Springer Nature remains neutral with regard to jurisdictional claims in published maps and institutional affiliations.